Journal of Theoretical Biology 354 (2014) 81–94

Contents lists available at ScienceDirect

Journal of Theoretical Biology

journal homepage: www.elsevier.com/locate/yjtbi

The dynamics of sperm detachment from epithelium in a coupled fluid-biochemical model of hyperactivated motility

Julie Simons [a,*], Sarah Olson [b], Ricardo Cortez [a], Lisa Fauci [a]

[a] Center for Computational Science and Mathematics Department, Tulane University, 6823 St. Charles Ave., New Orleans, LA 70118, USA
[b] Department of Mathematical Sciences, Worcester Polytechnic Institute, Worcester, MA 01609, USA

HIGHLIGHTS

- We examine the role that bonds and surfaces make in epithelial detachment of sper-matozoa in the oviduct.
- We propose two models for bond behavior at the epithelial surface and demonstrate the differences in detachment events.
- Considering forces alone is not sufficient to understand detachment and surface interactions.
- Both asymmetry and high amplitudes of the flagellar wave form are necessary for sperm to effectively break free of a surface.

ARTICLE INFO

Article history:
Received 6 December 2013
Received in revised form
7 March 2014
Accepted 14 March 2014
Available online 29 March 2014

Keywords:
Sperm motility
Hyperactivation
Stokes equations
Regularized Stokeslets

ABSTRACT

Hyperactivation in mammalian sperm is characterized by a high-amplitude, asymmetric flagellar waveform. A mechanical advantage of this hyperactivated waveform has been hypothesized to be the promotion of flagellar detachment from oviductal epithelium. In order to investigate the dynamics of a free-swimming sperm's binding and escaping from a surface, we present an integrative model that couples flagellar force generation and a viscous, incompressible fluid. The elastic flagellum is actuated by a preferred curvature model that depends upon an evolving calcium profile along its length. In addition, forces that arise due to elastic bonds that form and break between the flagellar head and the surface are accounted for. As in recent laboratory experiments, we find that a hyperactive waveform does result in frequent detaching and binding dynamics that is not observed for symmetric flagellar beats. Moreover, we demonstrate that flagellar behavior depends strongly on the assumptions of the bond model, suggesting the need for more experimental investigation of the biochemistry of epithelial bonding and the shedding of binding proteins on the sperm head.

1. Introduction

Successful fertilization in mammalian species requires sperm flagellar waveforms to change dramatically as the sperm travels through the female reproductive tract. One change that must occur is the transition from a symmetric, sinusoidal flagellar beatform to an asymmetric beatform with larger bending amplitudes along the flagellum, first observed in Yanagimachi (1970). Fig. 1 shows a series of micrographs of a bull sperm during active motility, transitional motility, and hyperactive motility (Marquez and Suarez, 2004). This intriguing motility change naturally raises the questions: What are the biochemical signaling pathways that initiate and maintain hyperactivation? Given these pathways, how is the internal dynein–microtubule force generation system of the flagellar axoneme altered to achieve this hyperactivated waveform? Moreover, what is the mechanical function of this hyperactivated waveform? As our focus is on the last question, we will consider the coupled system of a motile flagellum and a viscous, incompressible fluid.

Although there are still many open questions surrounding the details of the biochemistry of hyperactivation, it has been established that hyperactivation is mediated by calcium signaling pathways (Carlson et al., 2005; Ho et al., 2002; Suarez et al., 1993), and that mice whose sperm lack necessary membrane calcium (CatSper) channels do not exhibit hyperactivated motility and are infertile (Qi et al., 2007; Quill et al., 2003). Exactly how changes in calcium levels act to produce different bend patterns expressed by the axoneme is not known. It has been hypothesized that the asymmetric bending may be due to calcium binding directly to a subset of dynein arms (Lindemann and Kanous, 1995) or due to calcium binding to calmodulin receptors (Suarez, 2008).

* Corresponding author.
E-mail addresses: jsimons@tulane.edu (J. Simons), sdolson@wpi.edu (S. Olson), rcortez@tulane.edu (R. Cortez), fauci@tulane.edu (L. Fauci).

http://dx.doi.org/10.1016/j.jtbi.2014.03.024
0022-5193/

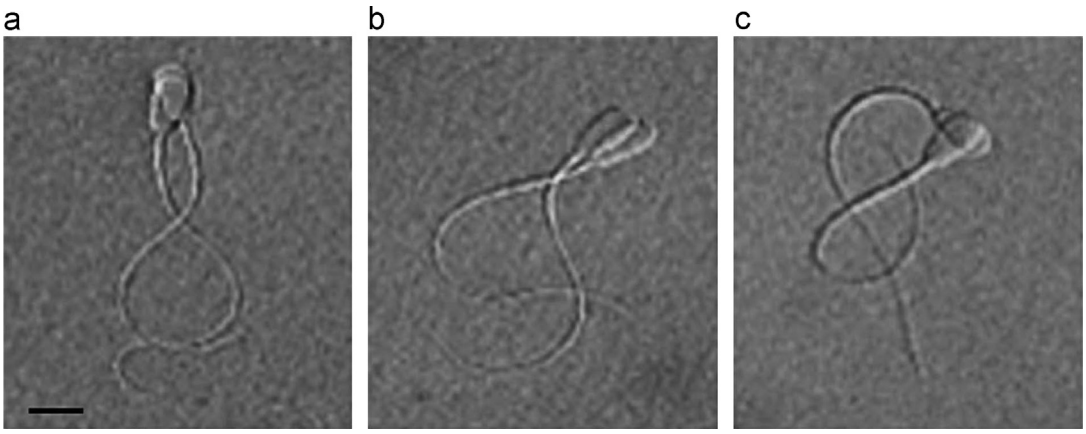

Fig. 1. Bull sperm exhibiting (a) activated motility, (b) hyperactivated motility, and (c) maximally hyperactivated motility. Reproduced with permission from Marquez and Suarez (2004).

In any case, the underlying biochemistry significantly alters the internal force generation to produce the observed hyperactive waveform. A mechanical advantage of this type of waveform has been hypothesized to be the generation of greater propulsive forces for the sperm to pass through the outer layers of the oocyte–cumulus complex (Alasmari et al., 2013; Quill et al., 2003; Stauss et al., 1995; Suarez and Dai, 1992; Suarez et al., 1991; Suarez, 2008). In addition to promoting penetration of the complex, viscoelastic matrix surrounding the oocyte, hyperactivated flagellar beating is hypothesized to enhance the sperm's ability to break free of the oviductal epithelium (DeMott and Suarez, 1992; Katz et al., 1989; Smith and Yanagimachi, 1991). Attachment occurs along cilia lining the epithelium and some candidates for binding receptors have been proposed (Baillie et al., 1997; Ignotz et al., 2007). Recently, it was confirmed that this motility pattern does accompany frequent attachment to and detachment from the oviductal epithelium in vivo (Chang and Suarez, 2012). This binding behavior is attributed to the forces generated by hyperactivation as well as the shedding of binding proteins on the head of the sperm, but the interplay between motility and protein shedding is unclear (Hung and Suarez, 2012; Pacey et al., 1995; Suarez et al., 2008; Suarez and Pacey, 2006). Sperm that do not undergo hyperactivation are unable to move through the oviduct (Ho et al., 2009).

While an asymmetric waveform of a free-swimming hyperactivated sperm results in a circular or curved trajectory (Yanagimachi, 1970), it may also generate both thrusting and tugging forces on a tethered sperm that could enable it to detach from a surface. To begin to address this question, a recent study (Curtis et al., 2012) considered a simple fluid dynamic model that calculated the total force generated by a filament with specified kinematics, clamped or freely hinged at the head. For a specified symmetric waveform with biologically realistic parameters, the total force at every phase of the wave was always a thrusting force, opposite the direction of the propagated wave. However, it was found that a specified asymmetric waveform could achieve total force both opposite the wave direction (thrust) and in the wave direction (tugging), depending upon the phase of the wave.

Motivated by the work in Curtis et al. (2012), here we present a model of the fully coupled system of an actuated, elastic filament in a three-dimensional Stokes fluid bounded by a planar wall. We use the preferred curvature model presented in Olson et al. (2011) that incorporates calcium dynamics to determine flagellar bending forces. We develop a model of sperm attachment to an epithelium layer by allowing elastic linkages between the planar boundary and the flagellum 'head' to form when the free-swimming flagellum comes within a threshold distance of the wall. In addition, detachment of the bound sperm can occur when the elastic linkage is stretched by the fluid beyond a given threshold. As in the recent experiments of Chang and Suarez (2012), we find that flagella with symmetric beat patterns (non-hyperactivated) tend to stay attached to the wall, and that hyperactivated flagella do dynamically attach and detach from the wall, and their resulting swimming trajectory may, indeed, allow them to swim away from the wall. While examining the resultant force for a given kinematic wave does give some insight about possible detachment, we see that other features, such as rotational motion of the flagellum induced by the wall and the nature of the elastic bonds, are essential mechanical elements contributing to the dynamics of flagellar detachment.

In the following sections, we will briefly describe the three-dimensional method of regularized Stokeslets (Ainley et al., 2008; Cortez et al., 2005) that allows us to couple the forces of the elastic flagellum with a Stokesian fluid in the presence of a planar wall. We will also briefly describe the coupled calcium, preferred curvature model of hyperactivation presented in Olson et al. (2011). We will present in detail the model of flagellar attachment and detachment to epithelia. We will show simulation results that examine the dynamics of a free-swimmer interacting with a planar surface, and discuss the differences observed for small amplitude, symmetric swimmers; large amplitude, symmetric swimmers; and hyperactivated swimmers whose waveform emerges from their internal calcium dynamics.

2. Stokes flow bounded by a plane wall

The velocity and length scales of sperm motility are small enough that inertial effects are negligible, with resulting Reynolds number on the order of 10^{-4}–10^{-2}. The governing fluid equations in this low Reynolds number regime are the incompressible Stokes equations:

$$\mu\Delta\mathbf{u} = \nabla p - \mathbf{F}(\mathbf{x})$$
$$\nabla\cdot\mathbf{u} = 0 \qquad (1)$$

with fluid velocity $\mathbf{u}$, dynamic viscosity μ, pressure p, and external force density (force per unit volume) $\mathbf{F}$. This force $\mathbf{F}$ represents the force that the sperm flagellum is exerting on the fluid. For simplicity, we will ignore the effects of the shape of the sperm head, which can vary widely in mammalian species. A slender filament such as a sperm flagellum can be approximated as a curve immersed in a fluid, exerting forces along its length. This system will be non-dimensionalized using characteristic scales listed in Table 1, which allow us to scale out the factor of μ in the equations.

Table 1
Characteristic scales used to non-dimensionalize the incompressible Stokes equations (1). The scales are chosen to be near those of typical mammalian sperm.

Quantity	Description	Value	Reference(s)
L	Length (sperm length)	100 μm	Cummins and Woodall (1985)
T	Time (from beat frequency)	0.1 s (10 Hz)	Ohmuro and Ishijima (2006), Smith et al. (2009b)
U	Velocity: wave speed, L/T	10^{-3} m/s	
	sperm body	$10^{-4}-10^{-5}$ m/s	Suarez and Dai (1992), Ohmuro and Ishijima (2006), Smith et al. (2009b)
μ	Viscosity (water)	10^{-3} kg m^{-1} s^{-1}	
P	Pressure $\left(\frac{\mu U}{L}\right)$	10^{-2} Pa	
F	Force density $\left(\frac{\mu U}{L^2}\right)$	10^{2} N/m^3	
Re	Reynolds number	$10^{-2}-10^{-4}$	

The coupled system of a force-generating flagellum and a Stokesian fluid results in a linear relationship between the velocities of material points along the flagellum and the forces exerted at those material points. For a free-swimming flagellum, the total force and torque along the flagellum must be zero. In order to analyze the fluid dynamics of this coupled system, one may approach the problem in two ways. If the kinematics of the flagellum are prescribed, the velocities of material points of the flagellum are known. Using these velocities, the forces required to generate those velocities may be calculated. The translational and rotational velocities of the flagellum result from enforcing the constraints that the motion be force- and torque-free. Alternatively, one may take as given the forces exerted along the flagellum. Given such a distribution of forces, the resulting fluid velocity field $\mathbf{u}$ may be calculated. The translation and rotation of the flagellum is achieved by allowing its material points to move at the resulting velocities at those points. In this second approach, the waveform of the flagellum is not prescribed, but emerges from the coupling between the prescribed forces and the surrounding viscous fluid.

Mathematical models that analyze resulting velocities and energy expenditure for prescribed flagellar kinematics have shed light upon many features of sperm motility in a Newtonian fluid, including, for instance, sperm accumulation near surfaces and the influence of head geometries (Smith et al., 2009a). Other models that capture fluid–structure interactions specify both passive and active forces along the flagellum (e.g. Gadêlha et al., 2010; Elgeti et al., 2010; Fu et al., 2008). These vary in the level of detail they seek to capture along with their chosen models of active force generation. For instance, the model of Gadêlha et al. (2010) treats the flagellum as an Euler–Bernoulli filament internally driven by an imposed wave of shear. More detailed models represent discrete collections of dynein motors that extend from one microtubule and dynamically attach and detach from the neighboring microtubule following curvature control activation theories (Dillon et al., 2007). In this paper, we choose a preferred-curvature model that treats the flagellum as an Euler-elastica internally driven by calcium-dependent forces (Olson et al., 2011). Whether forces or kinematics are prescribed, the implementation of a flagellar model relies on quantifying the linear relationship between fluid velocities and forces dictated by the Stokes equations. Resistive force theory, slender body theory, boundary integral methods, and immersed boundary methods are numerical treatments that vary in their simplifying assumptions and their ease of implementation. For discussions of both flagellar modeling and the numerical methods used to analyze these models, we point the reader to the review papers (Fauci and Dillon, 2006; Gaffney et al., 2011).

Here we choose a regularized Stokeslet formulation where forces are distributed along the length of the flagellum, but rather than assuming that these are point-forces, the force density is assumed to be given by $\mathbf{F}(\mathbf{x})=\mathbf{f}\phi_\delta(|\mathbf{x}|)$, where $\mathbf{f}$ is a vector coefficient and ϕ_δ is a smooth approximation of a delta function (also known as a blob function). Here, we use the following functional form:

$$\phi_\delta(r)=\frac{15\delta^4}{8\pi(r^2+\delta^2)^{7/2}}.$$

Other choices, such as Gaussian functions, are possible but the results are not strongly dependent on this choice. Using this regularized delta function, the velocity $\mathbf{u}$ for a set of forces $\mathbf{f}_k$ located at positions $\mathbf{x}_k$ is

$$\mathbf{u}(\mathbf{x})=\sum_{k=1}^{M}\left[\frac{\mathbf{f}_k(r_k^2+2\delta^2)+(\mathbf{f}_k\cdot(\mathbf{x}-\mathbf{x}_k))(\mathbf{x}-\mathbf{x}_k)}{8\pi(r_k^2+\delta^2)^{3/2}}\right] \tag{2}$$

where the radial distances are defined as $r_k=|\mathbf{x}-\mathbf{x}_k|$ and M is the number of forces along the flagellum.

We remark that the expression above tends to the classical sum of Stokeslets in the limit $\delta\to 0$. However, in this flagellar model we interpret the regularization parameter δ as a physical parameter that represents the radius of the flagellum. We also note that this velocity is an exact solution of the Stokes equations in three-space, and is exactly incompressible everywhere.

For flows bounded by a plane, the boundary condition $\mathbf{u}=0$ at the plane must be enforced. This can be done by defining an image point $\mathbf{x}_k^*$ associated with each position $\mathbf{x}_k$ by finding its reflection about the plane. Then, the no-flow boundary condition is satisfied by placing a Stokeslet, a Stokes doublet, a dipole and rotlets at the image point. The strength of each of these elements is computed from the original Stokeslet strength $\mathbf{f}$. The details of the implementation are described in Ainley et al. (2008). The final velocity formula has the form

$$\mathbf{u}(\mathbf{x})=\sum_{k=1}^{M}\left[\frac{\mathbf{f}_k(r_k^2+2\delta^2)+(\mathbf{f}_k\cdot(\mathbf{x}-\mathbf{x}_k))(\mathbf{x}-\mathbf{x}_k)}{8\pi(r_k^2+\delta^2)^{3/2}}\right]$$
$$-\left[\frac{\mathbf{f}_k(r_k^{*2}+2\delta^2)+(\mathbf{f}_k\cdot(\mathbf{x}-\mathbf{x}_k^*))(\mathbf{x}-\mathbf{x}_k^*)}{8\pi(r_k^{*2}+\delta^2)^{3/2}}\right]+\mathbf{u}_{sd}+\mathbf{u}_{pd}+\mathbf{u}_r. \tag{3}$$

The corresponding expressions for the Stokes doublets, dipoles and rotlets are denoted as $\mathbf{u}_{sd}+\mathbf{u}_{pd}+\mathbf{u}_r$ and the expressions for these velocities can be found in Ainley et al. (2008). In the next section we will discuss the preferred curvature model and its associated forces with which we couple Eq. (3) to find velocities $\mathbf{u}(\mathbf{x})$.

3. Preferred curvature model

As many mammalian species exhibit primarily planar flagellar beating patterns (Brokaw, 1965; Lindemann et al., 1992; Lindemann and Lesich, 2010), we model the motion of the sperm as a waveform restricted to the plane $z=0$. This waveform will evolve out of forces from a preferred curvature model developed in Fauci and Peskin (1988) and Olson et al. (2011). The forces that a sperm flagellum exerts are computed using a discretized version of the energy of a generalized Euler elastica:

$$E = \int_0^L (\varepsilon_{tens} + \varepsilon_{bend})\, ds \tag{4}$$

$$\varepsilon_{tens} = S_1 \left[\left\| \frac{d\mathbf{X}}{ds} \right\| - 1 \right]^2, \quad \varepsilon_{bend} = S_2 \left[\frac{\partial \Theta}{\partial s} - \zeta(s,t) \right]^2 \tag{5}$$

where $\mathbf{X}(s,t)$ is the centerline of the flagellum, L is its total length, s is the arc length and t is the time. The constants S_1 and S_2 are the tensile and bending stiffnesses, respectively, and are taken to be constant along the flagellum. The angle formed by the tangent to the flagellum and the head of the sperm is denoted by Θ. When discretized, the tensile energy density, ε_{tens}, can be thought of as an ideal spring model connecting the spatial positions along the flagellum. If the stiffness constant S_1 is large enough, the elements along the flagellum remain close to inextensible.

The bending energy density ε_{bend} penalizes sperm shapes whose curvatures deviate from their preferred curvature given by $\zeta(s,t)$. The resulting forces from these energy densities are calculated as

$$\mathbf{f} = -\frac{\partial}{\partial \mathbf{X}}(\varepsilon_{tens} + \varepsilon_{bend}). \tag{6}$$

We propose a sinusoidal curvature function ζ:

$$\zeta(s,t) = -b\kappa^2 \sin(\kappa s - \omega t)$$

to model the flagellar beating behavior. Since calcium dynamics are known to modulate the amplitude of flagellar beats (see Carlson et al., 2005; Ho et al., 2002; Suarez et al., 1993), the amplitude b of the curvature function ζ may also depend on local calcium concentrations along the flagellum.

To incorporate calcium dependence, the calcium concentration $C(s,t)$ evolves according to a one-dimensional reaction–diffusion model with spatially dependent fluxes incorporating the effects of calcium stores and channels along the flagellum (Olson et al., 2010, 2011):

$$\frac{\partial C}{\partial t} = D_c \frac{\partial^2 C}{\partial s^2} + J(s,t,C).$$

The effective diffusion coefficient is D_c and the flux of calcium into the sperm flagellum, $J(s,t,C)$ depends on both the location s along the sperm flagellum as well as the local calcium concentration. The chosen calcium model increases preferred amplitude and asymmetry as calcium levels increase inside the cytoplasm of the sperm, which is what is observed experimentally. Thus, we consider the following three forms for amplitude b in our analysis:

(A) *Symmetric case*: $b = b_0$ (a constant).

(B) *Simple asymmetric case*:

$$b = b_0 + k, \quad k = \begin{cases} k_1 & \text{if } \zeta(s,t) > 0 \\ -k_2 & \text{if } \zeta(s,t) \le 0 \end{cases}$$

where b_0 and k_i are non-negative constants and $k_2 < b_0$.

(C) *Calcium-dependent asymmetric case*:

$$b = \frac{V_0 C(s,t)}{C(s,t) + k_h}, \quad k_h = \begin{cases} k_+ & \text{if } \zeta(s,t) > 0 \\ k_- & \text{if } \zeta(s,t) \le 0 \end{cases}$$

where V_0 and $k_\pm$ are positive constants.

4. Results

We present the results of the curvature model for each motility behavior in three cases: without a wall, with a wall present, and with bond effects incorporated. Our model of the dynamics of bond formation and breaking will be discussed below. All parameters are listed in Table 2. We have taken the regularization parameter δ to be slightly larger than the radius of a flagellum.

For all simulations, the initial flagellar configuration is a straight line, with the sperm head placed at the origin, and the planar wall at $x = x_w = -0.01$. The flagellum is initialized in a

Table 2
Nondimensional parameter values used in models. Where noted, "prescribed" indicates parameters corresponding only to the prescribed position model (8). Parameters values have been chosen to match experimental data.

Parameter	Description	Value	Reference
δ	Regularization parameter	0.013	
Δs	Spatial (arc length) discretization	0.01	
L	Flagellum length	1	
b_0	Amplitude	0.1	Ohmuro and Ishijima (2006), Smith et al. (2009b)
κ	Wavelength parameter	2π	
ω	Frequency	1	
k_1	Asymmetry parameter for curvature	0.01	This work
k_2	Asymmetry parameter for curvature	0.02	This work
k_+	Activation parameter for Ca^{2+}-driven curvature	0.3	Olson et al. (2011)
k_-	Activation parameter for Ca^{2+}-driven curvature	0.5	Olson et al. (2011)
V_0	Ca^{2+}-driven amplitude scaling factor	0.45	Olson et al. (2011)
S_1	Tensile stiffness constant	100	Olson et al. (2011)
S_2	Bending stiffness constant	0.05	Olson et al. (2011)
S_3	Bond stiffness constant	100	This work
R_*	Bond resting length	0.01	This work
R_b	Bond breaking length	0.011	This work
R_c	Bond capture radius	0.0101	This work
K	Wavelength scaling factor (prescribed)	0.57	Curtis et al. (2012), Ohmuro and Ishijima (2006)
D	Amplitude scaling factor (prescribed)	4	Curtis et al. (2012), Ohmuro and Ishijima (2006)

plane perpendicular to the wall, and the direction of the wave of preferred curvature initially moves away from the wall. Due to symmetry and the form of the preferred curvature, the flagellum will always remain in the same plane. Moreover, because of the initial flat position of the flagellum, regular flagellar beating behavior takes some time to evolve into its natural waveform.

4.1. Simulations without a wall

Fig. 2 shows the position of three free-swimming flagella in three-space for a swimmer whose preferred curvature is (a) symmetric, (b) asymmetric and (c) calcium-driven. Note that the symmetric swimmer follows a straight path, on average, while the asymmetric swimmer moves along a circular path. The calcium-driven swimmer does not exhibit a regular path, as its preferred curvature is evolving in time.

In order to interpret the forces generated at the head of the sperm, a body frame of reference must be defined because freely swimming sperm will tend to rotate in space if they encounter an obstacle or have asymmetric waveforms. We define a centerline reference for the sperm using the position of the head of the sperm and the center of mass of the sperm. This should be thought of as an estimate of a body frame of reference; even in the symmetric case, this centerline direction will oscillate slightly. The center of mass is found by taking the spatial average of the flagellum points $\overline{\mathbf{X}}(t) = 1/M \sum_{k=1}^{M} \mathbf{X}_k(t)$, where M is the number of discretized material points along the flagellum. We define the centerline direction of the sperm to be

$$\mathbf{v_c} = \overline{\mathbf{X}}(t) - \mathbf{X}_1(t)$$

where the head of the sperm is located at $\mathbf{X}_1$. The transverse (normal) direction is defined accordingly in the plane $z=0$. We examine the forces of the free-swimmers shown in Fig. 2 in the centerline direction, without a wall or bond effects. Fig. 3(a) shows the evolution of the forces at the head for all three waveforms. One aspect to note here is that even in the symmetric case, there is a sign change in the force. This is not due to the centerline

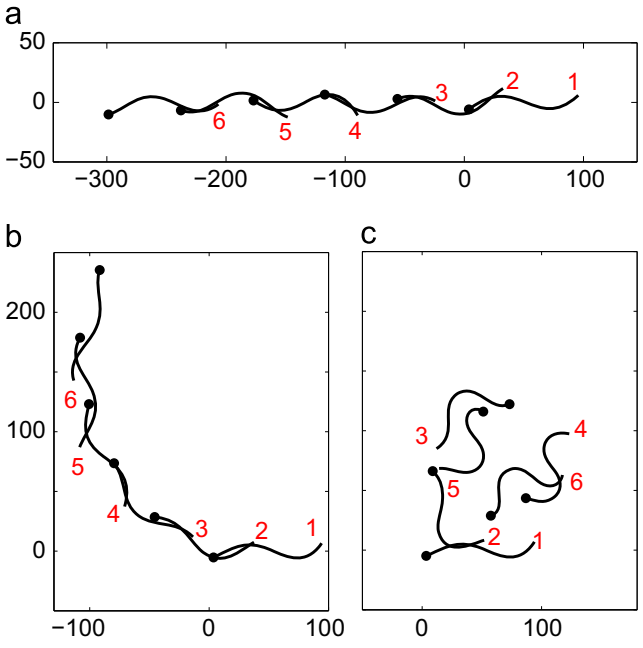

Fig. 2. Swimming behavior over time for different preferred curvature behaviors without a wall present. The head of the sperm is denoted by black dots, and numbers are placed at the tail of the flagellum to show the order of time progression in increments of approximately 9.825 beats. Spatial units are given in micrometers. These figures correspond to the supplemental movie M1.

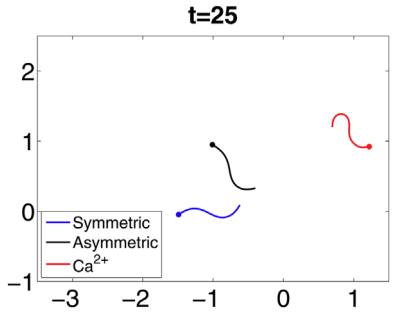

Movie M1. Movie of three different sperm motility behaviors in Stokes flow without a wall. Blue corresponds to the symmetric preferred curvature, black corresponds to the asymmetric preferred curvature, and red corresponds to the calcium-dependent asymmetric (hyperactive) preferred curvature. Each motility behavior is run separately and simulations are overlaid to demonstrate their differences. Dots correspond to the sperm heads. Units are non-dimensional, where a length of 1 and a time of 1 correspond to 100 μm and 10 seconds, respectively, in dimensional units. This movie corresponds to the sperm trajectories in Fig. 2. Supplementary material related to this article can be found online at http://dx.doi.org/10.1016/j.jtbi.2014.03.024.

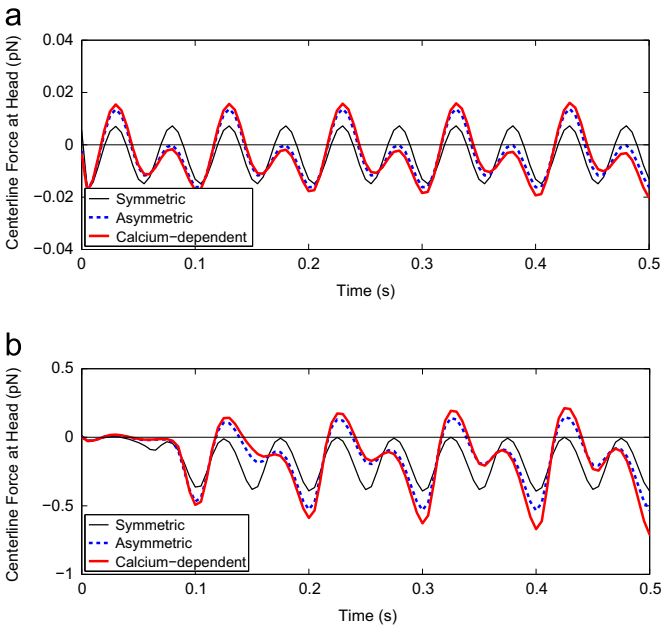

Fig. 3. The forces along the centerline generated at the head of the free-swimming sperm from preferred curvature model. Periodic flagellar beating takes some time to evolve into its natural waveform, which explains behavior near $t=0$. Time has been non-dimensionalized so that one beat corresponds to 1 unit in time for all waveforms. (a) The evolution of the centerline force of the free-swimmers with no wall shown in Fig. 2. (b) The evolution of the centerline force of the free-swimmers near a wall shown in Fig. 6. (a) No wall and (b) wall, no bond.

decomposition itself; a sign change is observed even when considering the standard x-component of forces, though it is less pronounced. The magnitudes of the forces for the calcium-dependent case are higher than the other cases, due to the higher amplitudes of the preferred curvature function.

4.2. Wall effects

To represent the oviductal epithelium, we use the method of images to incorporate a planar wall at $x = x_w$. Although it is assumed that the waveform and trajectory of the flagellum is confined to a plane, the resulting fluid velocity field is three-dimensional. Figs. 4 and 5 depict this velocity field surrounding the symmetric sperm flagellum near the wall.

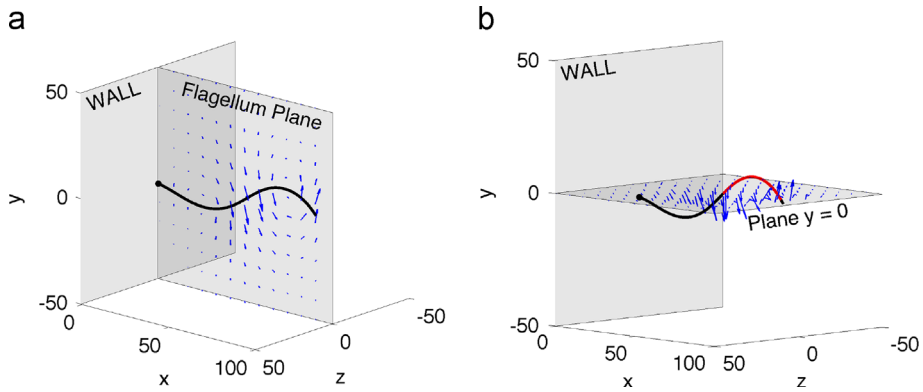

Fig. 4. A snapshot of the three-dimensional fluid flow around the flagellum and the wall, with spatial units given in micrometers. The red portion of the flagellum is above the plane $y=0$ in (b) on the right. (a) Flow field in $x-y$ plane and (b) flow field in $x-z$ plane. (For interpretation of the references to color in this figure caption, the reader is referred to the web version of this article.)

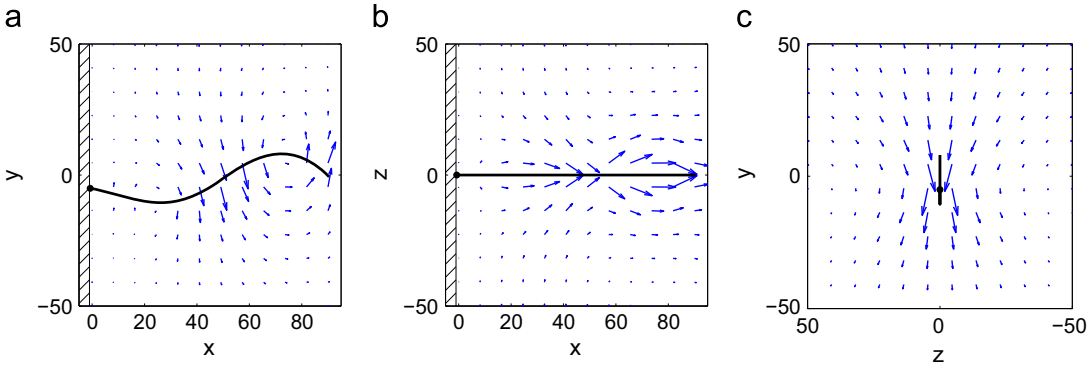

Fig. 5. Projected velocity fields due to beating flagellum shown on three orthogonal planes. Spatial units are given in micrometers. (a) Plane $z=0$, (b) plane $y=0$ and (c) plane $x=0.5$.

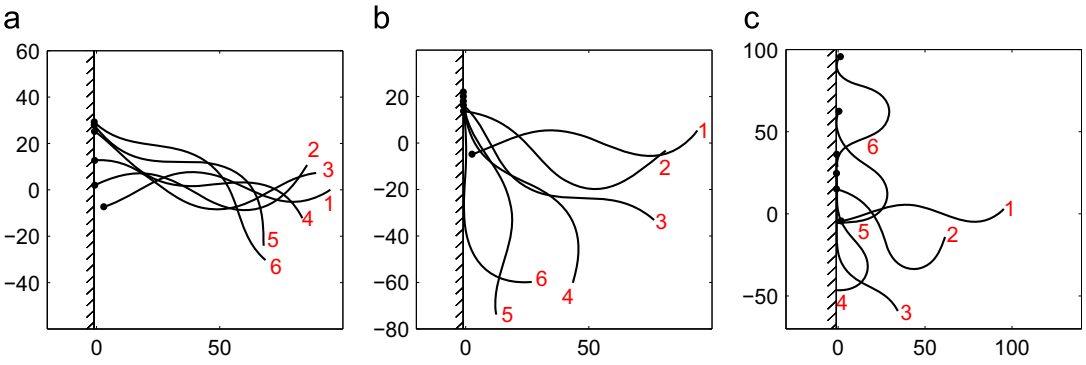

Fig. 6. The effect of a nearby wall on the dynamics of flagellar motility. Numbers are placed at the tail of the flagellum to show the order of time progression and the head of the sperm is denoted by black dots. Increment in position snapshots is approximately 9.825 beats for all figures, and spatial units are given in micrometers. The figures correspond to supplemental movie M2. (a) Symmetric, (b) asymmetric and (c) Ca^{2+}-dependent.

We now consider the dynamics of the free-swimmers shown in Fig. 2 when they are initially placed very close to the wall. Fig. 6 shows the position of these flagella near the wall over several periods of motion. The sperm body rotates and slowly drifts along the wall for all waveforms, regardless of asymmetry. The higher preferred curvature amplitudes in the calcium-dependent asymmetric model induce stronger forces that enable the sperm to progress further along the surface.

The addition of a planar wall has the effect of lowering the fluid velocities near the wall due to the no-slip boundary condition being satisfied exactly there. The swimmer cannot actually collide with the wall because the velocity field is a continuous function that transitions smoothly to zero at the wall, so the swimmer can only reach the wall asymptotically in time. The evolution of the force at the head in the direction of the centerline for each of these three free-swimmers is shown in Fig. 3(b). Here we see that the symmetric swimmer does not exhibit a sign change in force. While the asymmetric and calcium-driven swimmers do exhibit periodic sign changes in the centerline force, they do not succeed in swimming away from the wall. Fig. 3(b) also shows that, for these asymmetric swimmers, the wall increases the ratio of the maximum pushing force to maximum pulling force when compared to the ratio without the wall.

The preferred curvature models that actuate the swimmers in an unbounded fluid and those same swimmers near a planar wall in Figs. 2 and 6 are identical. However, because of fluid–structure

interactions, their achieved waveforms are not. We plot the emergent waveforms of each of these three swimmers, with and without a wall, in Fig. 7. Here the flagellum is translated and rotated to a body frame of reference. Note that the top row of Fig. 7 corresponds to Fig. 2 and the bottom row to Fig. 6. It is clear that a nearby surface can have significant effects on the sperm's achieved waveform.

For comparison to the results of Curtis et al. (2012), we consider the alternative regularized Stokeslet formulation that measures forces due to the prescribed kinematics of a flagellum. We consider the two waveforms:

$$y(x,t) = b_0 x \sin(\kappa x - \omega t) \quad \text{(symmetric case)} \tag{7}$$

$$y(x,t) = b_0 D x(\tau - \cos(K\kappa x - \omega t)) \quad \text{(hyperactive case)}. \tag{8}$$

These functional forms for the flagellum motion are non-dimensionalized in the same manner as our preferred curvature model. Both are sinusoidal waves with amplitudes growing from the head (at the origin) to the flagellar tip. The length of the body is a fixed arc length L. In the hyperactive waveform, τ is a "tilt" parameter which gives the flagellar waveform its asymmetry. If τ were taken to be zero, the hyperactive waveform would be equivalent to a symmetric wave. Fig. 8(a) and (b) shows the waveform envelopes created by (7) and (8).

To apply the method of images for regularized Stokeslets to calculate forces generated by the imposed motion (7) and (8), the velocities along the flagellum that these waveforms induce are needed. To accomplish this, a Newton method is used to find evenly distributed material points along the flagellar curve at every time step. This is necessary because all material points along the flagellum should have fixed arc length from the head, which ensures that the flagellum is inextensible. Maintaining these points as evenly distributed allows accurate calculation of both components of velocity that correspond to the specified flagellar centerline dynamics. To accomplish this, a center-difference formula in time is used to determine the velocities from the prescribed positions. The velocities at the material points of the flagellum are then used to solve for the forces that would give rise to the prescribed motion using the regularized Stokeslet linear system that relates the forces at the M discrete points on the flagellum to the velocity at these points governed by Eq. (3). Because the head is assumed to be tethered, the total force the flagellum exerts must be balanced by the force at the head. Fig. 8(c) shows the evolution of these forces for both waveforms,

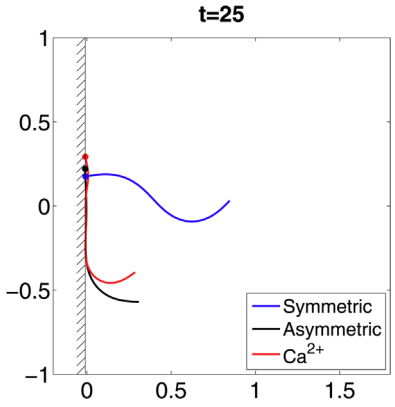

Movie M2. Movie of three different sperm motility behaviors in Stokes flow with a wall. Blue corresponds to the symmetric preferred curvature, black corresponds to the asymmetric preferred curvature, and red corresponds to the calcium-dependent asymmetric (hyperactive) preferred curvature. Each motility behavior is run separately and simulations are overlaid to demonstrate their differences. Dots correspond to the sperm heads. Units are non-dimensional, where a length of 1 and a time of 1 correspond to 100 μm and 10 seconds, respectively, in dimensional units. This movie corresponds to the sperm trajectories in Fig. 6.
Supplementary material related to this article can be found online at http://dx.doi.org/10.1016/j.jtbi.2014.03.024.

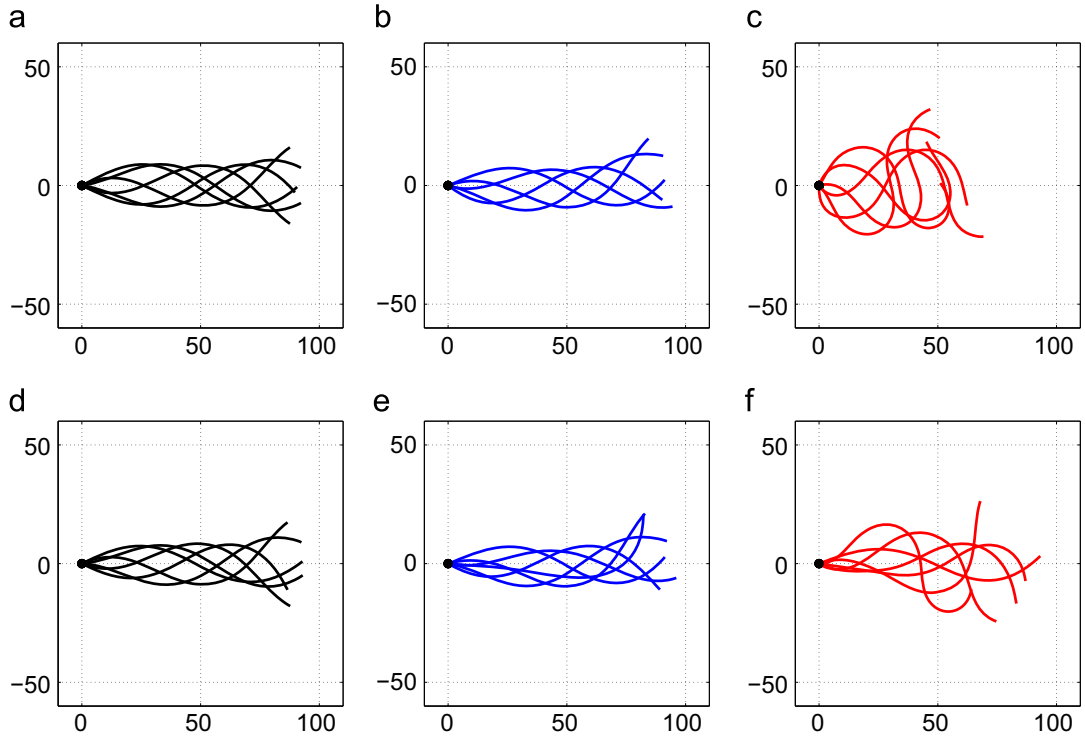

Fig. 7. Flagellar configurations evolved from preferred curvature model with parameters from Table 2, with units shown in micrometers. These configurations are translated to the centerline body frame of reference. (a) Symmetric, (b) asymmetric, (c) Ca^{2+}-dependent, (d) symmetric, with wall, (e) asymmetric, with wall and (f) Ca^{2+}-dependent, with wall.

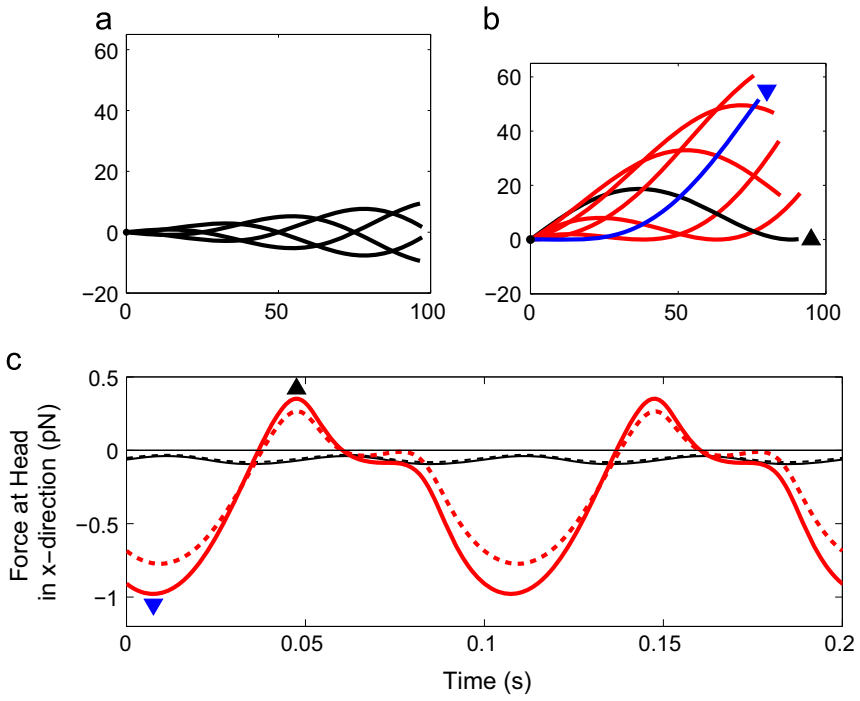

Fig. 8. Waveform envelopes and resulting forces for prescribed position models with parameters from Table 2. Panel (a) corresponds to the symmetric model (7) and panel (b) corresponds to the hyperactive model (8), with units shown in micrometers. In panel (b), the beat position labeled by ▾ corresponds to most negative (pushing) force generated at the head in the x-direction, and the beat position labeled by ▴ corresponds to the most positive (tugging) force generated in the x-direction. Panel (c) shows forces due to the prescribed waveforms in x computed using the method of regularized Stokeslets. Solid curves denote results when a wall is placed at $x=0$, and dashed curves show results without wall. Black curves are results from symmetric waveform (7) versus red curves from the hyperactive waveform, similar to those in Curtis et al. (2012). Tilt parameter is set as $\tau=1$. Triangles in panel (c) correspond to the flagellar positions labeled in panel (b). (For interpretation of the references to color in this figure caption, the reader is referred to the web version of this article.)

both with and without a wall placed at $x=0$. This figure compares well with the resistive force theory results presented in Curtis et al. (2012): when scaled in the same manner, our forces are within 10–20% of the values in Curtis et al. (2012) without a wall present. Since the planar wall is positioned in a different location in our model, the presence of the wall has a different effect. In Curtis et al. (2012), the presence of a nearby planar wall actually decreases the required force. We note that in our model the presence of the wall increases the forces required to maintain the waveform, similar to the results from the free-swimming, preferred curvature model presented above.

4.3. Bond effects

Dynamic, elastic linkages have been used in the context of immersed boundary models in biofluiddynamics to model, for example, platelet aggregation in blood clotting (Fogelson, 1984) and the action of dynein motors on microtubules in ciliary beating (Dillon and Fauci, 2000). In a similar manner, we model sperm binding to the oviductal epithelium by allowing an elastic linkage to form between the flagellum and the planar wall. This is done by adding a spring force at the head of the sperm when it comes within a capture radius R_c of the wall. This is a simple model for chemical bond formation when the binding proteins on the sperm head come close enough to the epithelial surface to bind. The material point of the flagellum at which this bond is attached evolves with the coupled fluid–flagellar system governed by the Stokes equations. Hence, the bond length also evolves with the flow dynamics. When this bond is stretched beyond a certain length R_b, the linkage is broken and the sperm freely swims as before. This Hookean force has strength

$$F_b = -S_3(R-R_*)$$

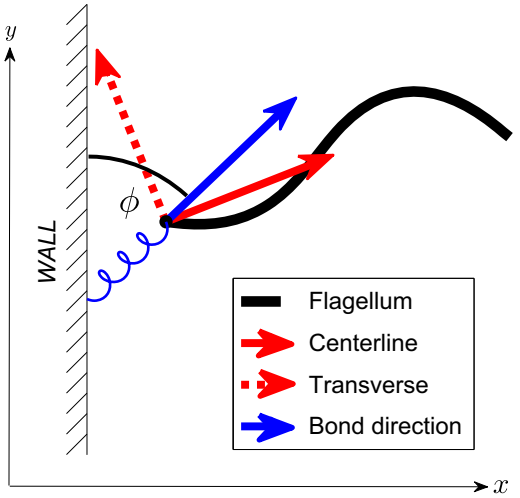

Fig. 9. Schematic for the geometry considered in a bound flagellum near a wall. The bond is depicted by the spring.

where R is the length of the spring (bond), R_* is its resting length, and S_3 is the stiffness constant. This force is applied at the head in the direction tangent to the bond. Note that this force resists both extension and compression of the bond away from its prescribed resting length.

The initial bond that forms between the sperm head and the wall will be oriented such that the other end of the spring is set at the point $(x_w, y^*, 0)$ when the wall is at $x = x_w$ and y^* is the y-coordinate of the head of the sperm at the time the bond is created. The bond direction, denoted by ϕ, will initially be $\pi/2$ and range from 0 to π as the head moves and the bond's attachment point to the wall $(x_w, y^*, 0)$ remains fixed (see Fig. 9). This models a pivoting spring

anchored at the wall. Typical bond behavior and associated distance between the head of the sperm and the wall is shown in Fig. 10 in a simulation where, initially, the head of the sperm is near the wall, and swimming towards it. As the head comes within the capture radius R_c, a bond is formed (as depicted by the red curve). This bond is formed with an initial length that is equal to the minimum distance between the sperm head and the wall, with a bond angle of $\phi = \pi/2$, but will fluctuate over time as the flagellum swims. This motion will both stretch and compress the bond, as well as rotate it (changing ϕ). When this bond length is stretched beyond a threshold breaking distance R_b, the bond is broken. This breaking event may be seen in Fig. 10, when the red curve surpasses the threshold R_b and the bond length immediately falls to 0 (meaning there is no bond present). If the sperm head again comes within a capture radius R_c, a new bond will be formed. This may happen instantaneously if the sperm stretches a bond while the sperm head is still within the capture radius of the wall itself. This is the type of behavior seen around times $t=1$ and $t=2$ in Fig. 10.

Fig. 11(a)–(c) shows the dynamics of the three free-swimmers previously shown in Figs. 2 and 6 with the inclusion of bond

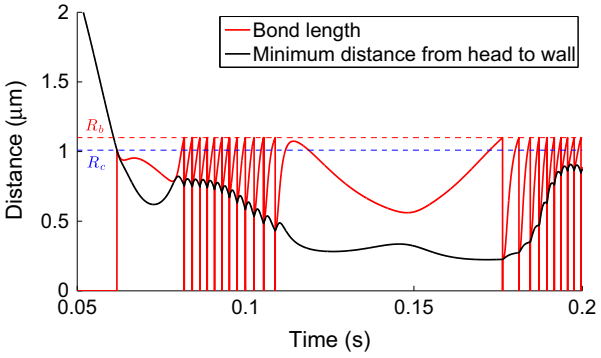

Fig. 10. Example of bond formation and breaking behavior as a sperm swims towards the wall, with bond capture radius R_c and constant breaking radius R_b. A bond length of 0 corresponds to a broken bond. (For interpretation of the references to color in this figure caption, the reader is referred to the web version of this article.)

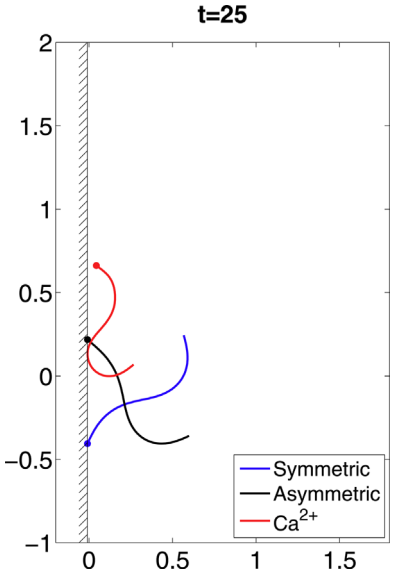

Movie M3. Movie of three different sperm motility behaviors in Stokes flow with a wall, with bond formation and bond parameter $\alpha = 0$. Blue corresponds to the symmetric preferred curvature, black corresponds to the asymmetric preferred curvature, and red corresponds to the calcium-dependent asymmetric (hyperactive) preferred curvature. Each motility behavior is run separately and simulations are overlaid to demonstrate their differences. Dots correspond to the sperm heads. Units are non-dimensional, where a length of 1 and a time of 1 correspond to 100 μm and 10 seconds, respectively, in dimensional units. This movie corresponds to the sperm trajectories in Fig. 11(a)–(c).
Supplementary material related to this article can be found online at http://dx.doi.org/10.1016/j.jtbi.2014.03.024.

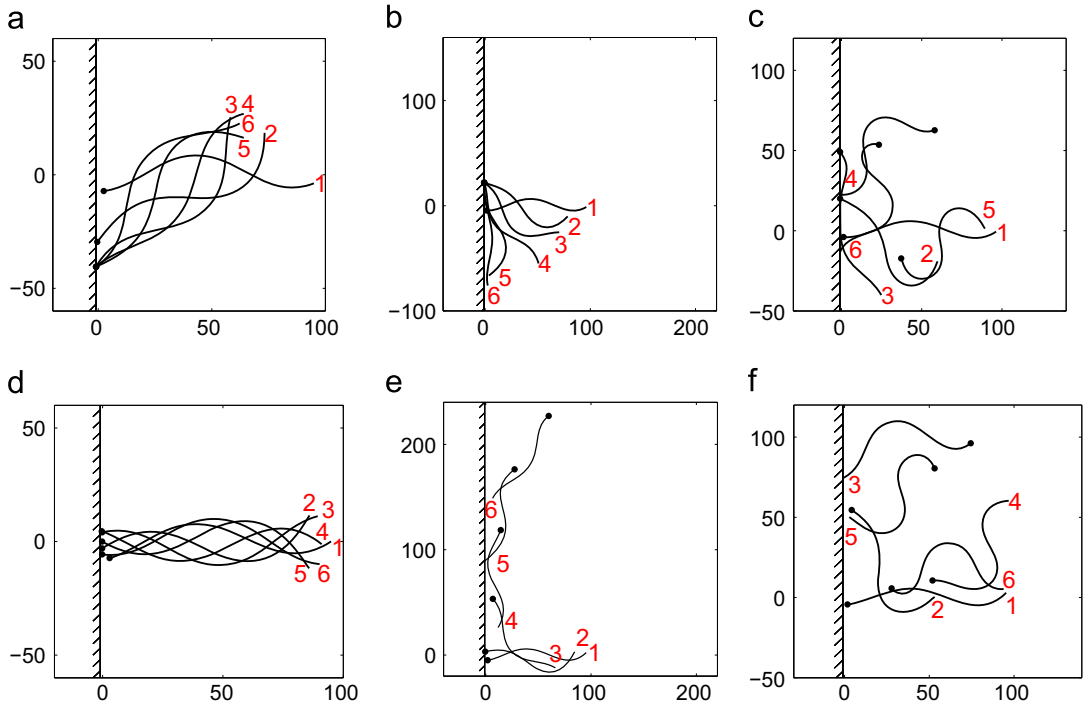

Fig. 11. Comparison of bond behaviors. Numbers are placed at the tail of the flagellum to show the order of time progression and the head of the sperm is denoted by black dots. The increment in position snapshots is approximately 9.825 beats for all figures, with spatial units given in micrometers. Note the ability of sperm to break free more quickly with the angular breaking condition. For comparison, all parameters and initial conditions are identical to those of Fig. 6. Supplemental movies M3 and M4 correspond to (a)–(c) and (d)–(f), respectively. (a) Symmetric, $\alpha=0$, (b) asymmetric, $\alpha=0$, (c) Ca^{2+}-dependent, $\alpha=0$, (d) symmetric, $\alpha=0.5$, (e) asymmetric, $\alpha=0.5$ and (f) Ca^{2+}-dependent, $\alpha=0.5$.

formation and detachment as described above. The symmetric waveform eventually settles into a steady beat pattern bound to the surface, though it is rotated away from the x-axis direction due to a symmetry-breaking effect of binding to the surface. We note that this rotation away from the x-axis depends upon what phase in the beat cycle the body is when bond formation occurs. The asymmetric waveform, on the other hand, lines up along the wall due to planar rotational effects caused by the beat asymmetry. As the bond aligns with the wall, even at its non-zero rest length, the forces generated by the beating flagellum are not high enough to allow the bond to break. The larger amplitude, asymmetric beating of the calcium-driven flagellum, however, does generate high enough forces to break free. This hyperactivated sperm in Fig. 11(c) breaks free and swims away in a curved path and then binds to the surface again.

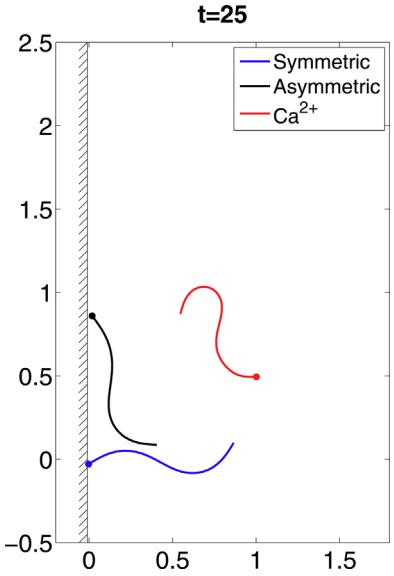

Movie M4. Movie of three different sperm motility behaviors in Stokes flow with a wall, with bond formation and bond parameter $\alpha=0.5$. Blue corresponds to the symmetric preferred curvature, black corresponds to the asymmetric preferred curvature, and red corresponds to the calcium-dependent asymmetric (hyperactive) preferred curvature. Each motility behavior is run separately and simulations are overlaid to demonstrate their differences. Dots correspond to the sperm heads. Units are non-dimensional, where a length of 1 and a time of 1 correspond to 100 μm and 10 seconds, respectively, in dimensional units. This movie corresponds to the sperm trajectories in Fig. 11(d)–(f).
Supplementary material related to this article can be found online at http://dx.doi.org/10.1016/j.jtbi.2014.03.024.

It is plausible that rotating significantly would break a bond. We extend our model of bond breaking to include angular dependence by introducing a parameter $\alpha(0\le\alpha\le1)$. The bond will break if its length exceeds the value:

$$[(1-\alpha)+\alpha\ \sin(\phi)]R_b. \tag{9}$$

When $\phi=\pi/2$, the breaking distance is R_b as it was before, but when ϕ approaches zero or π (the bond is aligning with the wall), the breaking distance is reduced to $(1-\alpha)R_b$. If $\alpha=0$, the condition is the original breaking condition with no angular dependence.

When angular effects are incorporated by setting $\alpha=0.5$, different behaviors can emerge, as shown in Fig. 11(d)–(f). The symmetric waveform maintains its relative orientation about the x-axis, regularly breaking and reforming bonds in a small region along the wall. Moreover, the asymmetric waveform is able to break free of the wall and avoid getting stuck despite its relatively small curvature amplitude. The calcium-dependent waveform breaks free of the surface more frequently but otherwise exhibits similar behavior to the $\alpha=0$ case. Fig. 12 highlights the difference that angular dependence of the bond has upon the trajectory of the position of the head of the sperm, showing the ability of the sperm to break free and swim away from the wall over time.

A comparison of the swimming behavior when bonds are present with the no-bond model in Section 4.2 highlights the significance of incorporating bond behavior. All initial conditions and parameters are identical for Figs. 6 and 11, which show results without and with bonds, respectively. Fig. 11 shows that regardless of angular effects in bond breaking, the bond can actually aid the sperm in overcoming the no-slip boundary condition effects observed in Fig. 6. This effect may seem counterintuitive, but arises because the bond force serves to keep the head some distance away from the wall due to the non-zero resting length. This enables the sperm head to move more readily. However, when the bond is able to freely rotate close enough to the wall (so that $\phi\approx0$ or π), the wall effect becomes apparent again and then the forces required to break the bond can become too large to achieve. When angular effects are incorporated, the bond effectively keeps the sperm head farther from the actual wall surface and the sperm body avoids the "capturing" effect of the no-slip boundary condition. These effects can be understood visually by examining the bond lengths and bond directions for the symmetric waveforms shown in Fig. 13. When $\alpha=0$, the bond can align with the wall, which does not occur when $\alpha=0.5$. While this is an idealized model for bond formation, it is clear that the choice of bond model has a significant impact upon behavioral outcomes.

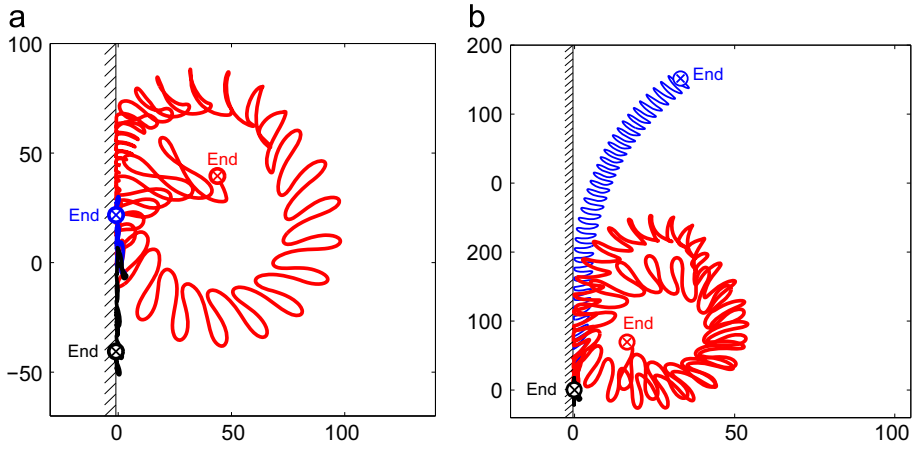

Fig. 12. Tracks of sperm head position for all waveforms, with bond behavior having (a) no angular dependence ($\alpha=0$) versus (b) $\alpha=0.5$. Black path is symmetric, blue is asymmetric, and red is Ca^{2+}-dependent. All heads start at (0, 0) and run over same simulation time length with end time positions indicated. Spatial units are given in micrometers. Supplemental movies M3 and M4 correspond to panels (a) and (b), respectively. (a) $\alpha=0$ and (b) $\alpha=0.5$. (For interpretation of the references to color in this figure caption, the reader is referred to the web version of this article.)

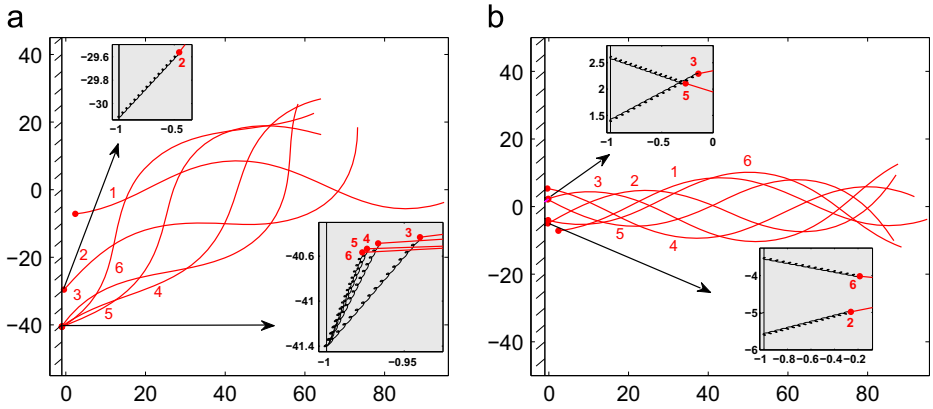

Fig. 13. Comparison of bond behavior for different values of bond parameter α for the symmetric waveform. Insets show the actual spring bond (black helical curves) and head locations in reference to the wall. Thus, in (a), we see the bond rotates very close to the wall as time progresses, indicating that the sperm head will experience a greater effect of the no-slip boundary condition. This issue is avoided in (b) since the breaking condition prevents alignment of the bond with the wall. Numbers are placed near flagellum to show the order of time progression where increment in position snapshots is approximately 9.825 beats for all figures, with spatial units given in micrometers. Wall location is at $x=-0.01$. (a) $\alpha=0$ and (b) $\alpha=0.5$.

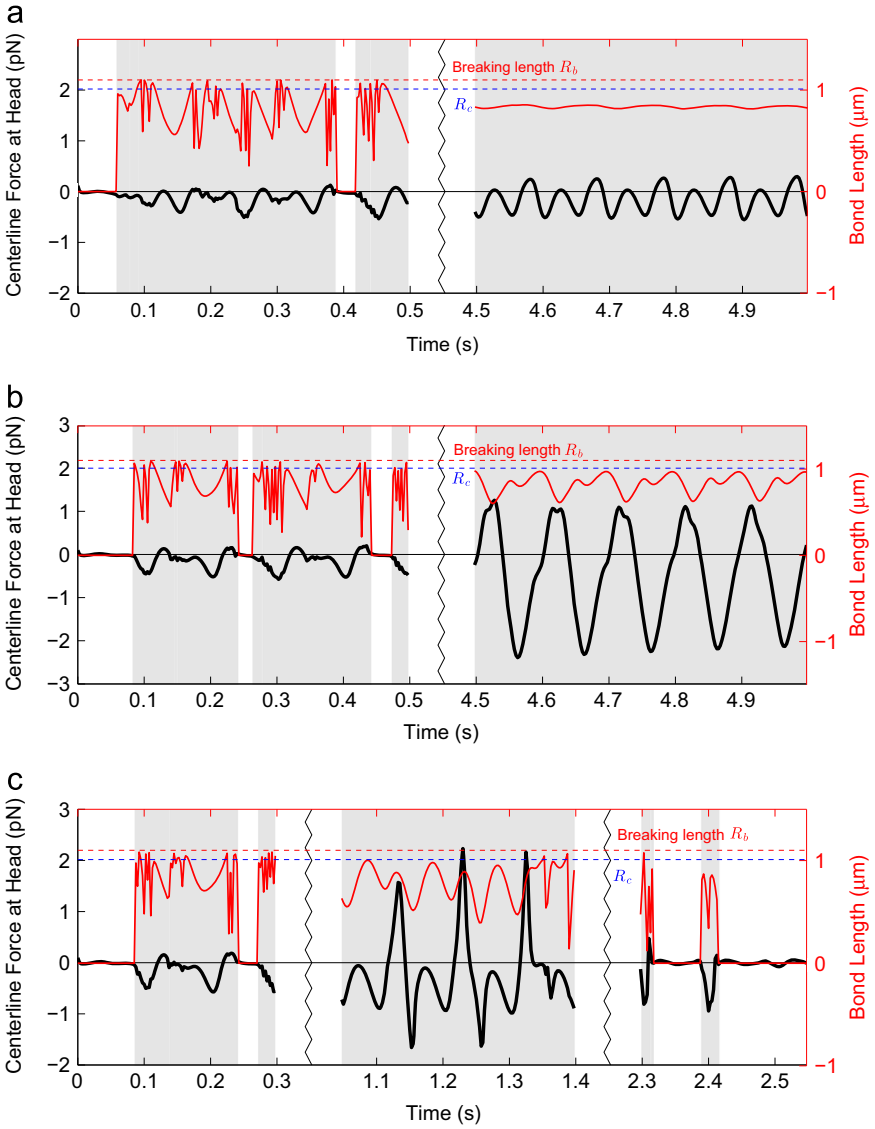

Fig. 14. Evolution of centerline forces at the head and bond lengths when $\alpha=0$. Bond formation and detachment occurs frequently due to the position of the head near the wall at early times, giving the forces more irregular jagged forms. Shaded regions are times when sperm is bound frequently (detachment events have a short duration). (a) Symmetric waveform, (b) asymmetric waveform and (c) calcium-dependent waveform.

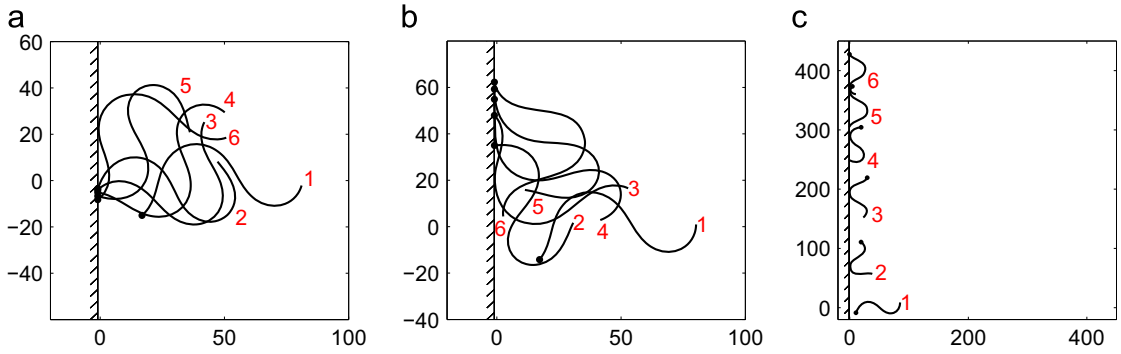

Fig. 15. Results for higher amplitude symmetric waveform, both without and with bond effects. Spatial units are given in micrometers. These figures correspond to supplemental movie M5. (a) No bond, (b) with bond, $\alpha=0$ and (c) with bond, $\alpha=0.5$.

The force at the head exhibits sign changes in the bond model as well. Fig. 14 shows the effect of adding a bond force upon the total force at the head over time, when angular effects are ignored. These plots correspond to the behaviors in Fig. 11(a)–(c). We plot the bond length as well to demonstrate bond behavior. For computational efficiency, data is not saved every time step, so the bond length data do not show every instance when the bond is stretched beyond the breaking distance. A length of zero corresponds to no bond. Frequent detachment and reattachment from the surface causes the force to appear more jagged. This is the behavior shown at earlier times in the plots corresponding to each of the three swimmers (left side). For the symmetric and asymmetric swimmers, we see that a persistent bond is formed for later times. In the calcium-dependent case, we see that a steady bond existed around time $t=24$, but it eventually breaks. Similar results are observed when angular effects are incorporated, except that bonds are broken more frequently (data not shown). In all cases, we note that sign changes occur in the centerline force at the head, both when persistent bonds are present or when they are not. We, therefore, cannot interpret epithelial detachment by examining this single force alone.

4.4. Large amplitude, symmetric swimmer

Since the calcium-dependent model in our parameter regimes exhibits the highest-amplitude behavior, one may ask whether the amplitude of the preferred curvature wave itself is enough to enable the sperm to generate a force large enough to break its surface bond, without any asymmetry. Fig. 15 shows a high amplitude, symmetric swimmer over time for all bond scenarios. Without bonds at all, large amplitude symmetric beats result in little drift along the wall (Fig. 15(a)). With bonds, larger amplitudes do, in fact, enable the sperm to progress along the wall as the bonds break and form (Fig. 15(b) and (c)). However, the symmetric waveform does not enable the requisite rotation to swim away from the surface. With angular dependence of bond breaking, $\alpha=0.5$, we do see a more pronounced progression along the surface. Thus, high amplitudes can enable surface detachment when bond behavior is incorporated, and result in a creeping behavior near the wall instead of movement of the flagellum away from the wall.

5. Discussion

Hyperactive behavior involving high amplitude, asymmetric waveforms can enable sperm to generate enough force to detach from a surface. Asymmetry alone may enable a weak bond with a surface to be broken, but the primary purpose of asymmetry is likely to enable the sperm to break free of a surface and swim away. Amplitude of the flagellar waveform is important for detachment. It has been previously

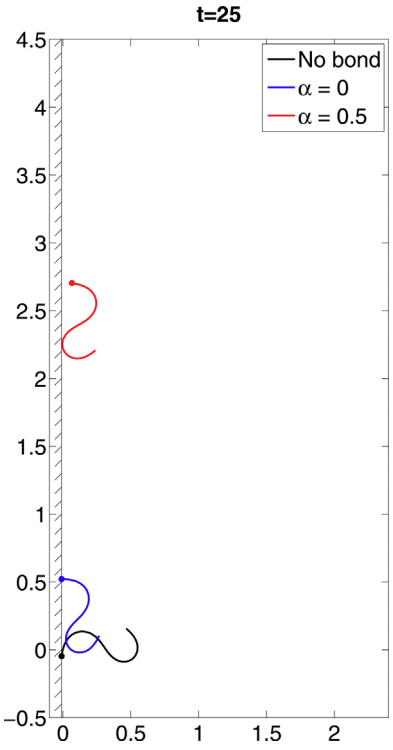

Movie M5. Movie of high amplitude symmetric motility behaviors in Stokes flow with a wall. Black corresponds to no bond formation, blue corresponds to bond formation with $\alpha=0$, and red corresponds to bond formation with $\alpha=0.5$. Each motility behavior is run separately and simulations are overlaid to demonstrate their differences. Dots correspond to the sperm heads. Units are non-dimensional, where a length of 1 and a time of 1 correspond to 100 μm and 10 seconds, respectively, in dimensional units. This movie corresponds to the sperm trajectories in Fig. 15.
Supplementary material related to this article can be found online at http://dx.doi.org/10.1016/j.jtbi.2014.03.024.

argued in Ishijima (2011) that high amplitude symmetric behavior might be an important feature in some sperm characterized as hyperactive. Our model suggests that high amplitude, symmetric waveforms allow progression along a wall, but would not allow a sperm to break free of the oviductal surface. Thus, the frequent detaching and binding dynamics observed in hyperactive sperm in vivo (Chang and Suarez, 2012) most likely relies upon both high amplitude and asymmetry.

It is clear that surface interactions have a large impact on the behavior of sperm, and the impact epithelial cilia have upon fertility is an ongoing area of investigation but has been shown to be important (Lyons et al., 2006). An interesting aspect of our model is that incorporating elastic bonding behavior at a surface

can actually *enable* sperm to move away from a wall. The non-zero resting length chosen for the bond between the flagellar head and the planar wall could be thought of as a simple model of the sperm binding to oviductal cilia (Petrunkina et al., 2001), which effectively keep the sperm head away from the surface and prevent the capturing effect of the no-slip boundary condition.

The choice of bond strength certainly affects the dynamics of flagellar detachment. Weakening the strength of the spring bond by lowering the stiffness parameter S_3 causes bonds to be formed and broken with much higher frequency. Conversely, increasing the spring stiffness makes it much more difficult for the sperm to break the bond and free itself from the surface. These effects could be modulated by changing the breaking condition given in Eq. (9) as well. Thus, these parameters serve to set both frequencies of detachment as well as a minimal force required over time to stretch the bond long enough to break it. We note that the scaling for forces involved in breaking bonds is on the order of several piconewtons (pN). We believe that this scaling is somewhat reasonable because bond strengths for some of the strongest known receptor–ligand pairs have been measured in the range of 5–170 pN (Florin et al., 1994; Merkel et al., 1999). The forces generated to break the bond are significantly higher than the forces at the head when there is no bond. It is possible that if we change the bond parameters, the sperm head would be able to achieve even higher forces due to our curvature model. Adjusting these parameters to fit experimental data such as that of Chang and Suarez (2012) is possible, but we would like to see the results of experiments that examine the bonding mechanisms more closely.

There is also heterogeneity in the behavior of sperm depending on the area of the oviduct they are bonded to: they frequently detach and reattach to the epithelium in the lower isthmus portion of the oviduct, whereas in the ampulla they remain attached for longer periods of time (Chang and Suarez, 2012), which may be related to the shedding of binding proteins. It is still unclear how all of these factors impact epithelial detachment, but they do suggest that bond and surface dynamics change as the sperm progresses through the oviduct.

There are several other aspects of hyperactive motility worth considering. One significant feature of hyperactivity in vivo is a decrease in beating frequency. Our current model specifies a beat frequency that does not depend upon the evolving calcium dynamics. We also have not taken into account any sort of energetic constraints related to the availability of ATP and other biological factors, which must play a role in sperm motility and may be one reason for decreased beating frequency and may have spatio-temporal effects along the flagellum itself. Additionally, we have idealized the flagellar beat to be restricted to one plane and, therefore, have not incorporated twisting or rolling behavior that sperm may be able to use to break their bonds. Recent work has highlighted the importance of considering three-dimensional waveforms in sperm, though mammalian sperm do appear to exhibit primarily planar waveforms and there is evidence that helical trajectories are suppressed in seminal plasma in mammalian sperm (Guerrero et al., 2011; Su et al., 2012, 2013). Our results indicate that surface interactions have a significant impact on flagellar behavior and therefore incorporating the ability for the flagellum to deviate from a planar form would be necessary for a more biologically realistic model, particularly with respect to more complex surfaces. Lastly, hyperactivity and oviductal detachment occurs near the time of ovulation (Ito et al., 1991; McNutt et al., 1994; Suarez et al., 2008) and environmental cues and oviductal fluid flow is certainly important. Here, we have ignored any background flows, which could be a factor in sperm progression. It is believed that chemotaxis as well as rheotaxis, or the ability of the sperm to sense direction of flow and swim against it, plays a significant role in enabling the sperm to successfully traverse the oviduct and reach the egg (Eisenbach, 1999; Friedrich and Jülicher, 2007; Miki and Clapham, 2013).

6. Conclusions

Hyperactivation in mammalian sperm motility is necessary for a sperm to reach and fertilize the egg. The specific role it plays during this complex process has been unclear, but it is speculated that hyperactivity enables sperm to escape mucosal folds in the oviduct and break bonds between the sperm head and the oviductal epithelium. In this model that couples a free-swimming flagellum in a viscous fluid with dynamic, elastic bonds to a planar wall, we demonstrate that a hyperactive waveform does enable the swimmer to break free of a surface. In addition, this model does capture the frequent detachment and reattachment observed in hyperactive sperm as opposed to the steady attachments observed in active, symmetrically beating sperm (Chang and Suarez, 2012). Our model uses a simple representation of the flagellum as an elastic filament, which is simplistic but allows for some understanding of the underlying physics. More detailed models that reflect the axonemal structure and dynein motor activation along the flagellum should be developed.

Epithelial bonding behavior and the shedding of binding proteins are still unresolved, but are current areas of investigation (Hung and Suarez, 2012; Suarez et al., 2008). This model highlights the need for further investigation into the nature of these surface bonds, as such bonds will have a significant hydrodynamic impact. We see that the overall dynamics in our model simulations are certainly dependent upon our choice of bond-detachment rules. Moreover, we have chosen here a generic mammalian sperm model, and have not tried to tailor it to a specific species. This model could provide a way to understand the effect of species-specific features and provide more insight into why species have evolved such different morphologies, binding capabilities, as well as motility patterns. These factors are all important in understanding fundamental questions in sperm fertility, infertility diagnoses and treatments, and may lead to insight in the evolution of sexual reproduction strategies.

Acknowledgments

The work of JS, RC and LF was supported, in part, by the National Science Foundation Grant DMS-104626, and the work of SO was supported, in part, by the National Science Foundation Grant DMS-1122461. The authors thank Susan Suarez for helpful discussions.

References

Ainley, J., Durkin, S., Embid, R., Boindala, P., Cortez, R., 2008. The method of images for regularized Stokeslets. J. Comput. Phys. 227 (9), 4600–4616.
Alasmari, W., Costello, S., Correia, J., Oxenham, S.K., Morris, J., Fernandes, L., Ramalho-Santos, J., Kirkman-Brown, J., Michelangeli, F., Publicover, S., et al., 2013. Ca^{2+} signals generated by catsper and Ca^{2+} stores regulate different behaviors in human sperm. J. Biol. Chem. 288 (9), 6248–6258.
Baillie, H., Pacey, A., Warren, M., Scudamore, I., Barratt, C., 1997. Greater numbers of human spermatozoa associate with endosalpingeal cells derived from the isthmus compared with those from the ampulla. Hum. Reprod. 12 (9), 1985–1992.
Brokaw, C., 1965. Non-sinusoidal bending waves of sperm flagella. J. Exp. Biol. 43 (1), 155–169.
Carlson, A.E., Quill, T.A., Westenbroek, R.E., Schuh, S.M., Hille, B., Babcock, D.F., 2005. Identical phenotypes of CatSper1 and CatSper2 null sperm. J. Biol. Chem. 280 (37), 32238–32244.
Chang, H., Suarez, S.S., 2012. Unexpected flagellar movement patterns and epithelial binding behavior of mouse sperm in the oviduct. Biol. Reprod. 86 (5).
Cortez, R., Fauci, L., Medovikov, A., 2005. The method of regularized Stokeslets in three dimensions: analysis, validation, and application to helical swimming. Phys. Fluids 17, 031504.
Cummins, J., Woodall, P., 1985. On mammalian sperm dimensions. J. Reprod. Fertil. 75 (1), 153–175.
Curtis, M., Kirkman-Brown, J., Connolly, T., Gaffney, E., 2012. Modelling a tethered mammalian sperm cell undergoing hyperactivation. J. Theor. Biol. 309, 1–10.

DeMott, R., Suarez, S.S., 1992. Hyperactivated sperm progress in the mouse oviduct. Biol. Reprod. 46 (5), 779–785.
Dillon, R., Fauci, L., 2000. An integrative model of internal axoneme mechanics and external fluid dynamics in ciliary beating. J. Theor. Biol. 207, 415.
Dillon, R., Fauci, L., Omoto, C., Yang, X., 2007. Fluid dynamic models of flagellar and ciliary beating. Ann. NY Acad. Sci. 1101 (1), 494–505.
Eisenbach, M., 1999. Sperm chemotaxis. Rev. Reprod. 4 (1), 56–66.
Elgeti, J., Kaupp, U.B., Gompper, G., 2010. Hydrodynamics of sperm cells near surfaces. Biophys. J. 99 (4), 1018–1026.
Fauci, L., Dillon, R., 2006. Biofluidmechanics of reproduction. Annu. Rev. Fluid. Mech. 38, 371–394.
Fauci, L.J., Peskin, C.S., 1988. A computational model of aquatic animal locomotion. J. Comput. Phys. 77 (1), 85–108.
Florin, E.-L., Moy, V.T., Gaub, H.E., 1994. Adhesion forces between individual ligand–receptor pairs. Science 264 (5157), 415–417.
Fogelson, A., 1984. A mathematical model and numerical method for studying platelet adhesion and aggregation during blood clotting. J. Comput. Phys 56, 111.
Friedrich, B.M., Jülicher, F., 2007. Chemotaxis of sperm cells. Proc. Natl. Acad. Sci. 104 (33), 13256–13261.
Fu, H., Wolgemuth, C., Powers, T., 2008. Beating patterns of filaments in viscoelastic fluids. Phy. Rev. E 78, 041913.
Gadêlha, H., Gaffney, E., Smith, D., Kirkman-Brown, J., 2010. Non-linear instability in flagellar dynamics: a novel modulation mechanism in sperm migration? J. R. Soc. Int. 7, 1689–1697.
Gaffney, E., Gadêlha, H., Smith, D., Blake, J., Kirkman-Brown, J., 2011. Mammalian sperm motility: observation and theory. Ann. Rev. Fluid Mech. 43, 501–528.
Guerrero, A., Carneiro, J., Pimentel, A., Wood, C.D., Corkidi, G., Darszon, A., 2011. Strategies for locating the female gamete: the importance of measuring sperm trajectories in three spatial dimensions. Mol. Hum. Reprod. 17 (8), 511–523.
Ho, H.-C., Granish, K.A., Suarez, S.S., 2002. Hyperactivated motility of bull sperm is triggered at the axoneme by Ca^{2+} and not cAMP. Dev. Biol. 250 (1), 208–217.
Ho, K., Wolff, C.A., Suarez, S.S., 2009. CatSper-null mutant spermatozoa are unable to ascend beyond the oviductal reservoir. Reprod., Fertil. Dev. 21 (2), 345–350.
Hung, P.-h., Suarez, S.S., 2012. Alterations to the bull sperm surface proteins that bind sperm to oviductal epithelium 1. Biol. Reprod. 87 (4).
Ignotz, G.G., Cho, M.Y., Suarez, S.S., 2007. Annexins are candidate oviductal receptors for bovine sperm surface proteins and thus may serve to hold bovine sperm in the oviductal reservoir. Biol. Reprod. 77 (6), 906–913.
Ishijima, S., 2011. Dynamics of flagellar force generated by a hyperactivated spermatozoon. Reproduction 142 (3), 409–415.
Ito, M., Smith, T., Yanagimachi, R., 1991. Effect of ovulation on sperm transport in the hamster oviduct. J. Reprod. Fertil. 93 (1), 157–163.
Katz, D.F., Drobnis, E.Z., Overstreet, J.W., 1989. Factors regulating mammalian sperm migration through the female reproductive tract and oocyte vestments. Gamete Res. 22 (4), 443–469.
Lindemann, C.B., Kanous, K.S., 1995. “Geometric clutch” hypothesis of axonemal function: key issues and testable predictions. Cell Motil. Cytoskelet. 31 (1), 1–8.
Lindemann, C.B., Lesich, K.A., 2010. Flagellar and ciliary beating: the proven and the possible. J. Cell Sci. 123 (4), 519–528.
Lindemann, C.B., Orlando, A., Kanous, K.S., 1992. The flagellar beat of rat sperm is organized by the interaction of two functionally distinct populations of dynein bridges with a stable central axonemal partition. Journal of Cell Sci. 102 (2), 249–260.
Lyons, R., Saridogan, E., Djahanbakhch, O., 2006. The reproductive significance of human fallopian tube cilia. Hum. Reprod. Updat. 12 (4), 363–372.
Marquez, B., Suarez, S.S., 2004. Different signaling pathways in bovine sperm regulate capacitation and hyperactivation. Biol. Reprod. 70 (6), 1626–1633.
McNutt, T.L., Olds-Clarke, P., Way, A.L., Suarez, S.S., Killian, G.J., 1994. Effect of follicular or oviductal fluids on movement characteristics of bovine sperm during capacitation in vitro. J. Androl. 15 (4), 328–336.
Merkel, R., Nassoy, P., Leung, A., Ritchie, K., Evans, E., 1999. Energy landscapes of receptor–ligand bonds explored with dynamic force spectroscopy. Nature 397 (6714), 50–53.
Miki, K., Clapham, D.E., 2013. Rheotaxis guides mammalian sperm. Curr. Biol. 23, 443–452.
Ohmuro, J., Ishijima, S., 2006. Hyperactivation is the mode conversion from constant-curvature beating to constant-frequency beating under a constant rate of microtubule sliding. Mol. Reprod. Dev. 73 (11), 1412–1421.
Olson, S.D., Suarez, S.S., Fauci, L.J., 2010. A model of CatSper channel mediated calcium dynamics in mammalian spermatozoa. Bull. Math. Biol. 72 (8), 1925–1946.
Olson, S.D., Suarez, S.S., Fauci, L.J., 2011. Coupling biochemistry and hydrodynamics captures hyperactivated sperm motility in a simple flagellar model. J. Theor. Biol. 283 (1), 203–216.
Pacey, A., Davies, N., Warren, M., Barratt, C., Cooke, L., 1995. Hyperactivation may assist human spermatozoa to detach from intimate association with the endosalpinx. Hum. Reprod. 10 (10), 2603–2609.
Petrunkina, A., Friedrich, J., Drommer, W., Bicker, G., Waberski, D., Topfer-Petersen, E., 2001. Kinetic characterization of the changes in protein tyrosine phosphorylation of membranes, cytosolic Ca^{2+} concentration and viability in boar sperm populations selected by binding to oviductal epithelial cells. Reproduction 122 (3), 469–480.
Qi, H., Moran, M.M., Navarro, B., Chong, J.A., Krapivinsky, G., Krapivinsky, L., Kirichok, Y., Ramsey, I.S., Quill, T.A., Clapham, D.E., 2007. All four catsper ion channel proteins are required for male fertility and sperm cell hyperactivated motility. Proc. Natl. Acad. Sci. 104 (4), 1219–1223.
Quill, T.A., Sugden, S.A., Rossi, K.L., Doolittle, L.K., Hammer, R.E., Garbers, D.L., 2003. Hyperactivated sperm motility driven by CatSper2 is required for fertilization. Proc. Natl. Acad. Sci. 100 (25), 14869–14874.
Smith, D., Gaffney, E., Blake, J., Kirkman-Brown, J., 2009a. Human sperm accumulation near surfaces: a simulation study. J. Fluid Mech. 621 (1), 289–320.
Smith, D., Gaffney, E., Gadêlha, H., Kapur, N., Kirkman-Brown, J., 2009b. Bend propagation in the flagella of migrating human sperm, and its modulation by viscosity. Cell Motil. Cytoskelet. 66 (4), 220–236.
Smith, T., Yanagimachi, R., 1991. Attachment and release of spermatozoa from the caudal isthmus of the hamster oviduct. J. Reprod. Fertil. 91 (2), 567–573.
Stauss, C.R., Votta, T.J., Suarez, S.S., 1995. Sperm motility hyperactivation facilitates penetration of the hamster zona pellucida. Biol. Reprod. 53 (6), 1280–1285.
Su, T.-W., Choi, I., Feng, J., Huang, K., McLeod, E., Ozcan, A., 2013. Sperm trajectories form chiral ribbons. Sci. Rep. 3.
Su, T.-W., Xue, L., Ozcan, A., 2012. High-throughput lensfree 3D tracking of human sperms reveals rare statistics of helical trajectories. Proc. Natl. Acad. Sci. 109 (40), 16018–16022.
Suarez, S., Dai, X., 1992. Hyperactivation enhances mouse sperm capacity for penetrating viscoelastic media. Biol. Reprod. 46 (4), 686–691.
Suarez, S., Katz, D., Owen, D., Andrew, J., Powell, R., 1991. Evidence for the function of hyperactivated motility in sperm. Biol. Reprod. 44 (2), 375–381.
Suarez, S., Pacey, A., 2006. Sperm transport in the female reproductive tract. Hum. Reprod. Updat. 12 (1), 23–37.
Suarez, S.S., 2008. Control of hyperactivation in sperm. Hum. Reprod. Updat. 14 (6), 647–657.
Suarez, S.S., Varosi, S.M., Dai, X., 1993. Intracellular calcium increases with hyperactivation in intact, moving hamster sperm and oscillates with the flagellar beat cycle. Proc. Natl. Acad. Sci. 90 (10), 4660–4664.
Suarez, S.S., et al., 2008. Regulation of sperm storage and movement in the mammalian oviduct. Int. J. Dev. Biol. 52 (5–6), 455–462.
Yanagimachi, R., 1970. The movement of golden hamster spermatozoa before and after capacitation. J. Reprod. Fertil. 23 (1), 193–196.